






Weyl nodal loop semimetals and tunable quantum anomalous Hall states in two-dimensional ferromagnetic cerium monohalides

Shu-Zong Li , Jun-Shan Si , Zhixiong Yang , and Wei-Bing Zhang *

Hunan Provincial Key Laboratory of Flexible Electronic Materials Genome Engineering, School of Physics and Electronic Sciences, Changsha University of Science and Technology, Hunan, Changsha 410114, China

 (Received 27 November 2023; revised 3 February 2024; accepted 29 February 2024; published 13 March 2024)

Quantum anomalous Hall (QAH) effect with dissipationless edge channels offers innovative insight for designing the next-generation low-power electronic devices. Based on first-principles calculations and the tight-binding (TB) model, we predict rich QAH states with a tunable Chern number in single-layer ferromagnetic cerium monohalides CeX ($X = \text{Cl, Br, I}$). These stable ferromagnetic single-layer materials have isotropic magnetocrystalline anisotropy in the x - y plane, which favors the adjustment of the topological state with an external magnetic field. A distinct Weyl nodal loop exists in the band structure of the CeX single layers without spin-orbit coupling (SOC). When SOC is included and all mirror symmetries are broken, QAH state can be realized. Intriguingly, QAH states with varying Chern number ($C = \pm 1$), two-dimensional Weyl semimetals and band gap periodically manifest as the magnetization direction rotates in the x - y plane. Furthermore, A TB model based on Slater-Koster framework is constructed to explain the origin of nontrivial band structure in CeX single layers. The CeX single layers exhibit remarkable topological states, providing an excellent platform for exploring low-power spintronic devices.

DOI: [10.1103/PhysRevB.109.115418](https://doi.org/10.1103/PhysRevB.109.115418)

I. INTRODUCTION

Topological quantum materials with exotic properties offer tremendous potential for realizing the next-generation electronic devices [1,2]. Quantum anomalous Hall (QAH) effect features dissipationless chiral channels on the edge of the samples. The quantity and chirality of these channels are determined by the absolute value and the sign of the Chern number, respectively [3,4]. Augmenting the absolute value of the Chern number implies an increase in the number of dissipationless channels. Manipulating the positive and negative signs of the Chern number corresponds to controlling the conduction directions of these channels, which provides a unique platform for designing chiral logic low-power electronic devices. Most of the materials proposed to realize quantum anomalous Hall (QAH) effect have out-of-plane magnetizations and fixed Chern numbers [5–13]. It is interesting to explore the QAH states with in-plane magnetizations and tunable Chern numbers.

Based on the tight-binding (TB) model and group theory analysis, nonzero Chern numbers in two-dimensional (2D) materials can only be realized when all mirror symmetries, $\mathcal{T} \otimes M_z$ and $\mathcal{T} \otimes M_z \otimes \mathcal{I}$, are broken, where \mathcal{T} , M_z , and \mathcal{I} represent time reversal, out-of-plane mirror (i.e., $z \rightarrow -z$), and inversion symmetry, respectively [4,14,15]. These conditions are usually satisfied for the out-of-plane magnetization, but not always true for in-plane magnetization. For instance, a QAH state can be found in 2D material CsAs [16], where a QAH state emerges with out-of-plane magnetization but is absent with in-plane magnetization.

Nowadays, some QAH insulators with in-plane magnetizations and tunable Chern numbers have also been predicted [17–25]. These available candidates primarily focus on Dirac spin-gapless semiconductors, which possess fully spin-polarized Dirac points at the Fermi energy and can transition into QAH insulators when spin-orbit coupling (SOC) is considered [26–28]. Therefore, it is significant to further generalize the QAH state to different topological state precursors and structures. As one of quantum materials, nodal-line semimetals (NLSMs) can be viewed as precursors of other topological states [29,30]. Magnetic Weyl NLSMs with broken \mathcal{T} exhibit twofold degenerate band crossings of nodal lines [16,31–35]. They also provide an excellent platform for systematically investigating the tunable QAH state and its underlying mechanisms.

In this paper, we theoretically investigate tunable QAH states in a series of 2D single-layer cerium monohalides CeX ($X = \text{Cl, Br, I}$), which are 2D Weyl NLSMs without SOC. The stability, magnetic property, electronic structure, and topological properties of CeX single layers are given in detail. These materials have isotropic magnetocrystalline anisotropy energy in the x - y plane and can realize tunable QAH states or 2D Weyl semimetals via manipulating the magnetization direction. A multiorbital tight-binding (TB) model in Slater-Koster framework is further constructed to understand the origin of nontrivial electronic properties in CeX single layers. These materials provide a great platform for investigating exotic topological physics in materials.

II. COMPUTATIONAL METHODS

The first-principles calculations were performed in the Vienna *ab initio* simulation package (VASP) [36,37] with

*zhangwb@csust.edu.cn

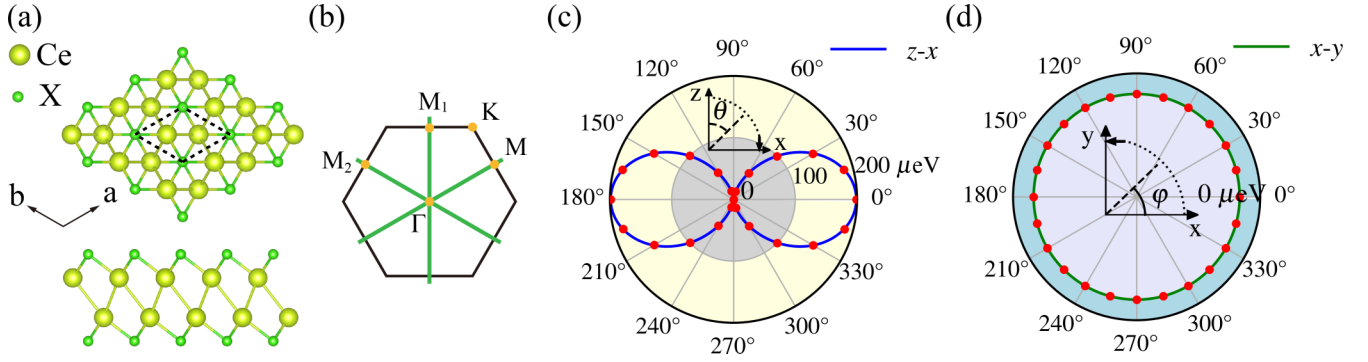


FIG. 1. The crystal structure, Brillouin zone of CeX single layers, and Magnetocrystalline anisotropy energy (MAE) of the CeCl single layer. (a) Top and side views of the crystal structure of CeX single layers visualized by VESTA [50]. The dotted lines represent primitive cell. (b) The Brillouin zone of CeX single layers. The yellow dots represent high-symmetry points, and green lines represent mirror planes perpendicular to x - y plane. (c), (d) MAE of the CeCl single layer as a function of the polar angle θ and the azimuthal angle ϕ , respectively. The red dots represent the first-principles calculations, and the solid lines represent the fitted curves.

the projector augmented-wave (PAW) method [38,39]. The generalized gradient approximate (GGA) of the Perdew-Burke-Ernzerhof (PBE) functional [40] is adopted as an exchange-correlation functional. The Brillouin zone is sampled in $16 \times 16 \times 1$ Γ -centered k point grids by the scheme of Monkhorst-Pack [41]. The cutoff energy of the plane-wave basis set is 500 eV, and the energy convergence criterion is 10^{-6} eV. The unit cell and atoms are optimized until the forces on all atoms are less than 0.01 eV/Å. To avoid the interaction between two adjacent layers, a vacuum layer of at least 20 Å is included in the structure. The $5s^2 6s^2 5p^6 5d^1 4f^1$ electrons of Ce and p electrons of X ($X = \text{Cl, Br, and I}$) atoms are regarded as valence electrons. The f electrons of Ce are treated as core electrons in phonon spectrum calculation. To account for Coulomb interaction for f electrons, the density functional theory (DFT) + U methods are adopted [42] with effective Hubbard parameters $U_{eff} = U - J = 4$ eV, which refers to the recommended value in rare earth metal oxides CeO₂ [43]. The phonon spectrum is calculated using the PHONOPY package with the finite displacement approach [44], in which a $4 \times 4 \times 1$ supercell is used. The d orbitals of Ce are used to construct the maximally localized Wannier functions (MLWFs) by Wannier90 software [45], and related calculations of topological properties are performed by WannierTools [46] and the VASPBERRY code [47,48]. The magnetic point groups of structure when SOC is included is computed by FINDSYM [49].

III. CRYSTAL STRUCTURE, STABILITY, AND MAGNETIC PROPERTY

Bulk CeBr was found to be van der Waals layered material in early experiments [51], indicating that the corresponding single-layer material can be obtained by exfoliation. The crystal structure of CeX single layers is shown in Fig. 1(a). Two layers of Ce are sandwiched between the two sides of halogen (X), and Ce atoms are arranged in a low-buckled honeycomb structure. The space group of CeX single layers is $P\bar{3}m1$ (No. 164), and the corresponding point group is D_{3d} , which possesses threefold rotational symmetry along the z axis C_{3z} , \mathcal{I} , and in-plane twofold rotational symmetry C_2 . These generators result in 12 symmetry operations, including

three mirror symmetries perpendicular to the x - y plane, as shown in Fig. 1(b). The optimized lattice parameters of CeX single layers are summarized in Table I.

To reveal the dynamical stability of CeX single layers, we investigate their phonon spectrums. As shown in Fig. S1 in the Supplemental Material [52], the imaginary frequency is absent in the whole Brillouin zone, which indicates all three CeX single layers are dynamically stable. Furthermore, We perform molecular dynamics simulations at 300 K in a canonical ensemble using the Nosé-Hoover heat bath scheme to study the thermal stability of the CeX single layers. Although there are thermal-induced fluctuations, the structures of CeX single layers are not destroyed, indicating that the CeX single layers are thermally stable at room temperature (see Fig. S2 [52]).

Magnetic properties are essential in ferromagnetic materials [53,54]. The magnetic moments of CeX single layers are mainly contributed by f and d electrons of Ce, and the values of magnetic moments are not integer, approximately $3.7 \mu_B$, as shown in Table I. By comparing the total energies of four possible magnetic configurations, including ferromagnetic (FM), Néel antiferromagnetic (NAFM), stripy antiferromagnetic (SAFM), and zigzag antiferromagnetic (ZAFM) configurations (see Fig. S3 and Table S1 [52]), the magnetic ground states of all CeX single layers are ferromagnetic.

To obtain insights of the magnetic anisotropy, we also calculated the energies of CeX single layers with the different magnetization directions in the z - x and x - y planes. The polar angle θ is the angle between magnetization \mathbf{m} and the z direction in the z - x plane, while azimuthal angle ϕ is the angle

TABLE I. The lattice constant a , magnetic moment, and magnetocrystalline anisotropy energy (MAE). The MAE is defined as the energy difference between z and x magnetization directions.

CeX	a (Å)	Magnetic moments (μ_B)	MAE (meV)
CeCl	4.01	3.728	199
CeBr	4.07	3.702	27
CeI	4.18	3.684	-420

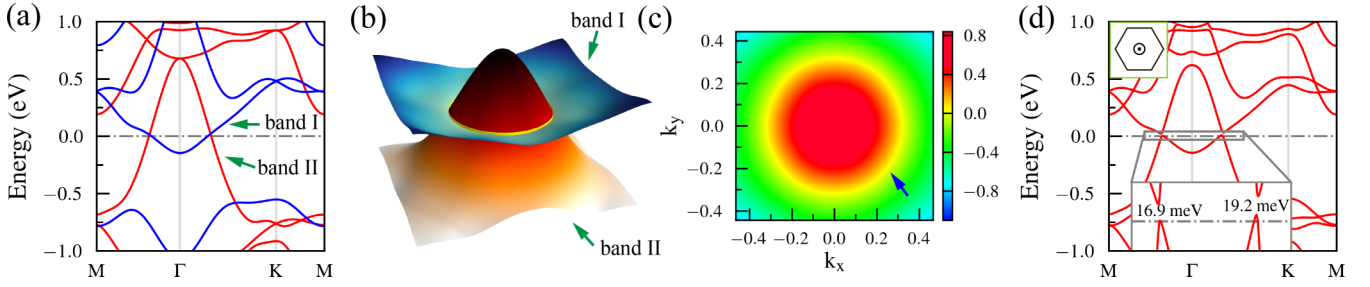


FIG. 2. The band structure of the CeCl single layer without/with SOC. (a) Spin-polarized band structure of the CeCl single layer. The red (blue) bands lines denote spin-down (spin-up) bands. (b) The 3D band structure of the CeCl single layer without SOC near the Fermi energy. The yellow loop indicates the Weyl nodal loop. (c) The difference between the band II and the band I. The position where the value is zero is the Weyl nodal loop, and the yellow loop shows the profile of the Weyl nodal loop in the 2D Brillouin zone. (d) The band structure of the CeCl single layer with SOC when the magnetization direction is $\theta = 0^\circ$ (z direction).

between magnetization \mathbf{m} and the x direction in the x - y plane. The magnetocrystalline anisotropy energy (MAE) is defined as $\text{MAE}(\theta, \varphi) = E(\theta, \varphi) - E(\theta = 90^\circ, \varphi = 0^\circ)$, where the value of θ and φ range from 0° to 360° . Figure 1(c) shows MAE when there is different magnetization of CeCl single layer in the z - x plane, and MAE can be fitted as $\text{MAE}(\theta) = K_0 \cos^2(\theta) + K_1 \cos^4(\theta)$ [55], where K_0 and K_1 are $198.03 \mu\text{eV}$ and $0.75 \mu\text{eV}$, respectively. It can be found that MAE reaches the minimum when polar angle is equal to 90° (270°), which indicates that the magnetization of the CeCl single layer is more inclined along the x direction. Figure 1(d) further illustrates that the CeCl single layer has isotropic magnetization in the x - y plane and belongs to XY ferromagnets [56]. The CeBr and CeI single layers also have isotropic magnetization in the x - y plane, but the magnetization of the CeI single layer in the ground state is out of plane. The in-plane isotropic magnetization provides an excellent platform for quantum manipulation by the magnetic field.

IV. BAND STRUCTURE AND TOPOLOGICAL STATE

We further investigate the band structures of CeX single layers. Since band structures of CeX single layers are very similar, we use the CeCl single layer as demonstration example. The spin-polarized band structure of the CeCl single layer without SOC is shown in Fig. 2(a). We find that the electronlike conduction band I contributed by spin-down channel (blue band) and the holelike valence band II contributed by spin-up channel (red band) form two obvious twofold degenerate band crossings near Fermi energy, and form a Weyl nodal loop around the Γ point. The three-dimensional band structure of these two inverted bands is shown in Fig. 2(b), which further verifies the Weyl nodal loop semimetal state in the CeCl single layer. The profile of the Weyl nodal loop in the 2D Brillouin zone is shown in Fig. 2(c). The position where two bands intersect clearly form a loop. Further analysis indicates that the Weyl nodal loop is mainly contributed by d_{z^2} , $d_{x^2-y^2}$ and d_{xy} orbitals of Ce (see Fig. S4 [52]).

Next, we investigate the effect of different magnetization directions on the Weyl nodal loop when SOC is considered. When the magnetization direction is $\theta = 0^\circ$ (z direction), then only the \mathcal{I} and C_{3z} parallel to the magnetization remain in the system. Because the entire Weyl nodal loop is not

protected by additional symmetry, the Weyl nodal loop is gapped. Especially, the band gaps in the high-symmetry paths Γ -M and Γ -K are 16.9 meV and 19.2 meV , respectively, as shown in the inset of Fig. 2(d).

An intriguing phenomenon occurs with periodic variation in band gap and topological states as the magnetization is rotated in the x - y plane, as shown in Fig. 3. When the magnetization direction is in the x - y plane, the SOC band gap of the degenerate point in the high-symmetry paths depends on the broken degree of the corresponding symmetry [25]. The band gap of the Weyl nodal loop in the path Γ -M (Γ -M₁ and Γ -M₂) located on the mirror symmetries depends on the angle between \mathbf{m} and the corresponding paths, i.e., the degree of the corresponding broken mirror symmetry. When the magnetization direction is $\varphi = 0^\circ$ (60° , 120° , 180° , 240° , and 300°), the mirror symmetry perpendicular to \mathbf{m} is preserved, resulting in the band in the corresponding path is gapless, and the CeCl single layer is a 2D Weyl semimetal. When the magnetization direction is $\varphi = 30^\circ$ (90° , 150° , 210° , 270° , and 330°), the mirror symmetry parallel to \mathbf{m} is broken to the greatest extent, which leads to a maximum band gap of 17.3 meV along this mirror symmetry. As φ rotates from 0° to 360° , the value of the SOC band gap (g) in these high-symmetry paths can be

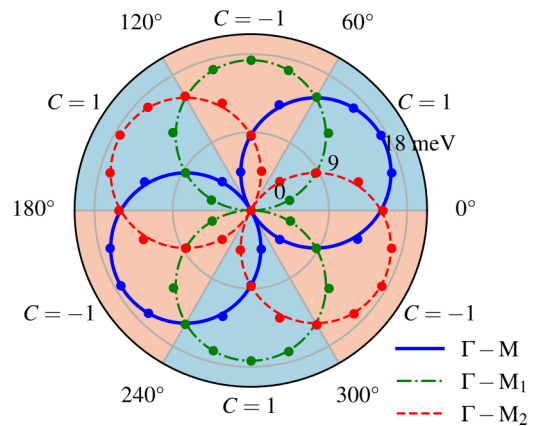


FIG. 3. The value of band gap in high-symmetry paths Γ -M (Γ -M₁ and Γ -M₂) and the sign of the Chern number as a function of azimuthal angle φ in the x - y plane. Lines and dots represent fitted curves and DFT calculations, respectively. Orange (blue) areas correspond to Chern number $C = +1$ ($C = -1$).

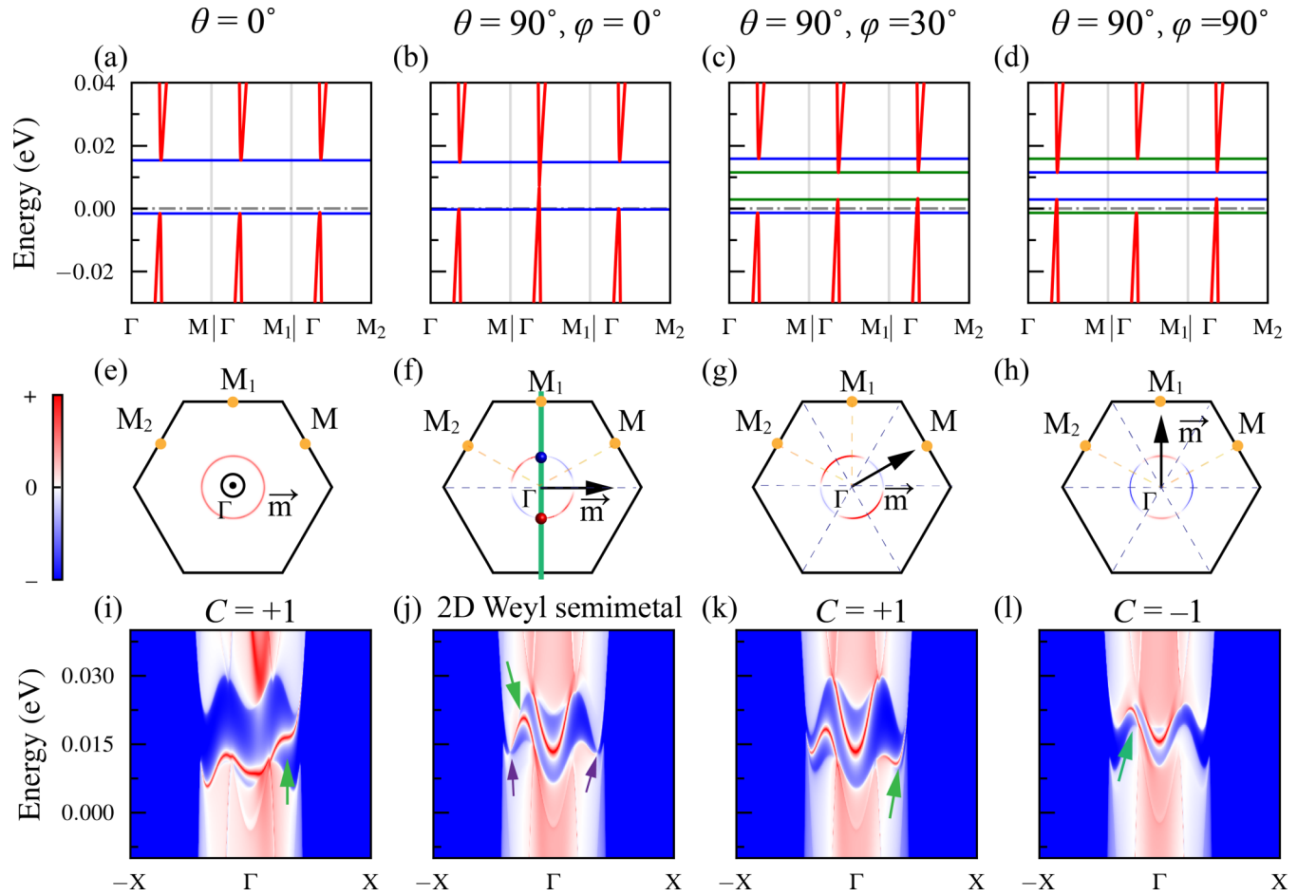


FIG. 4. The band structures, Berry curvatures, and edge states with different magnetization direction. (a)–(d) Band structures in high-symmetry paths Γ -M, Γ -M₁, and Γ -M₂ with SOC. (e)–(h) The distributions of Berry curvatures, where the green line, blue and red dots denote mirror plane, Weyl points with topological charge ν of -1 and 1 , respectively. (i)–(l) Edge states along the zigzag direction. (a) [(e) and (i)], (b) [(f) and (j)], (c) [(g) and (k)], and (d) [(h) and (l)] correspond to the cases when the direction of magnetization \mathbf{m} (black arrow) are $\theta = 0^\circ$ (z direction), $\varphi = 0^\circ$ (x direction), $\varphi = 30^\circ$, and $\varphi = 90^\circ$ (y direction), respectively.

described as $g = 17.3 \times |\cos(\varphi - \alpha)|$ meV, where Γ -M, Γ -M₁, and Γ -M₂ correspond to $\alpha = 30^\circ$, 90° , and 150° , respectively. Our DFT calculations fit this functional relationship well, as shown in Fig. 3. Importantly, as the magnetization direction rotates in the x - y plane, the closing and reopening of the band gap is accompanied by the Chern number switching between $+1$ and -1 with a period of 60° .

We next illustrate the interplay among magnetization, symmetries, and band gap using example with the out-of-plane ($\theta = 0^\circ$) and the in-plane ($\varphi = 0^\circ$, 30° and 90°) magnetization directions. When the magnetization direction is $\theta = 0^\circ$, C_{3z} symmetry is preserved by the pseudovector \mathbf{m} , making the band gaps in the paths Γ -M, Γ -M₁, and Γ -M₂ the same (between the two blue lines), as shown in Fig. 4(a). When the magnetization direction is $\varphi = 0^\circ$ (x direction) in the x - y plane, the pseudovector \mathbf{m} will not break the mirror symmetry perpendicular to it, which leads to the band in path Γ -M₁ is not gapped ($0 = \cos 90^\circ \times 17.3$ meV), as shown in Fig. 4(b). Considering \mathcal{I} , the Weyl nodal loop without SOC degenerates into a pair of Weyl points. The band gaps in the path Γ -M and Γ -M₂ are both $15.0 \approx \cos 30^\circ \times 17.3 \approx |\cos 150^\circ| \times 17.3$ meV (between the two blue lines), where 30° , 90° , and 150° are the angles between \mathbf{m} and paths

Γ -M, Γ -M₁, and Γ -M₂, respectively. When the magnetization direction is $\varphi = 30^\circ$ in the x - y plane, the Weyl nodal loop is gapped because all mirror symmetries except \mathcal{I} are broken. In Fig. 4(c), the band gap in the path Γ -M is $17.3 = \cos 0^\circ \times 17.3$ meV (between the blue lines), and the band gap in the Γ -M₁ and Γ -M₂ are both $8.6 \approx \cos 60^\circ \times 17.3 \approx |\cos 120^\circ| \times 17.3$ meV (between the green lines), where 0° , 60° , and 120° are the angles between \mathbf{m} and paths Γ -M, Γ -M₁, and Γ -M₂, respectively. When the magnetization direction is $\varphi = 90^\circ$ (y direction) in the x - y plane, the band gap in the path Γ -M₁ is $17.3 = \cos 0^\circ \times 17.3$ meV (between the green lines), and the band gap in the paths Γ -M and Γ -M₂ are both $8.6 \approx \cos 60^\circ \times 17.3$ meV (between the blue lines), where 60° , 0° , and 60° are the angles between \mathbf{m} and paths Γ -M, Γ -M₁, and Γ -M₂, respectively, as shown in Fig. 4(d).

The gap of Weyl nodal loop results in nonzero Berry curvatures, and transforms the system into a QAH state. For the out-of-plane magnetization, the Berry curvatures in the 2D Brillouin zone are positive and Chern number $C = +1$, as shown in Fig. 4(e). When the magnetization direction is $\varphi = 0^\circ$, half of Berry curvatures in the 2D Brillouin zone are positive and the remaining are negative, which just cancel each other out. Besides, a topological charge defined as the

Berry phase of a counterclockwise closed loop around the Weyl points can be written as [25,57,58]

$$\nu = \frac{1}{\pi} \oint_{\ell} \mathbf{A}(\mathbf{k}) \cdot d\mathbf{k},$$

where $\mathbf{A}(\mathbf{k})$ is the Berry connection. The topological charge ν of the Weyl point (blue dot) in the path Γ - M_1 is -1 , whereas the ν of other Weyl point (red dot) is $+1$, as shown in Fig. 4(f). When the magnetization direction is $\varphi = 30^\circ$ in the x - y plane, four-sixths of Berry curvatures are positive, and the remaining two-sixths are negative. The Berry curvatures distribution for $\varphi = 90^\circ$ is opposite of $\varphi = 30^\circ$, as shown in Figs. 4(g) and 4(h). The opened Weyl nodal loop induces the QAH state with Chern number ($C = \pm 1$) and is also proved by the evolution of Wannier charge centers (WCCs), as shown in Fig. S5 [52]. The edge state of the CeCl single layer can be obtained by using the constructed semiinfinite system, as shown in Figs. 4(i), 4(j), 4(k), and 4(l). In the QAH state, a distinct edge state (indicated by the green arrow) connects the conduction and valence bands. Additionally, for the 2D Weyl semimetal, there is an extra pair of twofold degenerate Weyl points (indicated by the purple arrow), as shown in Fig. 4(j).

It is widely accepted that the sign of the Chern number depends on the direction of the relative spin. When the magnetization direction is $\varphi = 30^\circ$ (90° , 150° , 210° , 270° , and 330°), the magnetic point group of the CeCl single layer is $2'/m'$ that lacks $\mathcal{T} \otimes \mathcal{M}_z$ and $\mathcal{T} \otimes \mathcal{M}_z \otimes \mathcal{I}$. The spin direction of the CeCl single layer is equivalent to the same at $\varphi = 30^\circ$, 150° , and 210° . This equivalence is also at $\varphi = 90^\circ$, 210° , and 330° , but the spin directions of $\varphi = 30^\circ$ and $\varphi = 90^\circ$ are equivalently opposite, as shown in Fig. S6 [52]. Therefore, The Chern number of $\varphi = 30^\circ$ (150° and 270°) and $\varphi = 90^\circ$ (210° and 330°) are opposite signs. As mentioned above, the isotropic in-plane magnetization is found in the CeX single layers, which makes it easy to realize the transition between positive and negative Chern numbers.

V. TIGHT-BINDING MODEL

As discussed in the previous DFT calculation, the contribution of the Weyl nodal loop is mainly contributed by the d orbitals of Ce. To explain the origin of nontrivial band structure in CeX single layers, we constructed the nearest neighbor (NN) tight-binding model based on the Slater-Koster framework and the orthogonal basis $\{|d_{z^2}\rangle, |d_{x^2-y^2}\rangle, |d_{xy}\rangle, |d_{yz}\rangle, |d_{xz}\rangle\} \otimes \{|\uparrow\rangle, |\downarrow\rangle\}$ for the CeCl single layer [15,59–62]:

$$H = \sum_{i\alpha} \epsilon_{i\alpha} c_{i\alpha}^\dagger c_{i\alpha} - \sum_{i\alpha, j\beta} t_{ij, \alpha\beta} c_{i\alpha}^\dagger c_{j\beta} + \lambda_{SO} \sum_i c_{i\alpha}^\dagger \mathbf{L} \cdot \boldsymbol{\sigma} c_{i\beta} + t_m \sum_{i\alpha} c_{i\alpha}^\dagger \mathbf{m} \cdot \boldsymbol{\sigma} c_{i\alpha},$$

where $c_{i\alpha}^\dagger = (c_{i\alpha\uparrow}^\dagger, c_{i\alpha\downarrow}^\dagger)$ creates an electron at the i th site, \uparrow (\downarrow) and α represent spin up (down) and the α orbital, respectively. The first term is on-site energy, and d orbitals of Ce are split into three groups: d_0 (d_{z^2}), d_1 ($d_{x^2-y^2}$, d_{xy}), and d_2 (d_{yz} , d_{xz}) due to the D_{3d} point group. The second term is the NN hopping energy with amplitude $t_{ij, \alpha\beta}$, which is given in Table II by the Slater-Koster formula. The third term is

TABLE II. The Slater-Koster (SK) tight-binding parameters of the CeCl single layer. The SK parameters are obtained by fitting DFT band structure excluding the f orbitals, exchange field \mathbf{m} , and SOC [63,64]. Unit: eV.

$\epsilon_{d_{z^2}}$	$\epsilon_{d_{x^2-y^2}, d_{xy}}$	$\epsilon_{d_{yz}, d_{xz}}$	$V_{dd\sigma}$	$V_{dd\pi}$	$V_{dd\delta}$
1.345	3.370	0.320	0.880	0	0.152

on-site SOC with strength λ_{SO} , where $\boldsymbol{\sigma} = (\sigma_x, \sigma_y, \sigma_z)$ and $\mathbf{L} = (L_x, L_y, L_z)$ are the Pauli operator and angular momentum operator, respectively. The explicit expression of this term is [60]

$$H_{SO} = \lambda_{SO} \begin{pmatrix} 0 & 0 & 0 & i\sqrt{3}\sigma_x & -i\sqrt{3}\sigma_y \\ & 0 & -2i\sigma_z & i\sigma_x & i\sigma_y \\ & & 0 & i\sigma_y & -i\sigma_x \\ \text{H.c.} & & & 0 & i\sigma_z \\ & & & & 0 \end{pmatrix}.$$

The last term is the on-site exchange coupling with magnetization strength t_m , where $\mathbf{m} = (\sin\theta\cos\varphi, \sin\theta\sin\varphi, \cos\theta)$.

By transforming this Hamiltonian from real space to momentum space \mathbf{k} and numerically solving the eigenvalue equation, the band structure of the TB model for the CeCl single layer is obtained. Figure 5 shows the evolution of the band structure with exchange field \mathbf{m} and SOC. Figure 5(a)

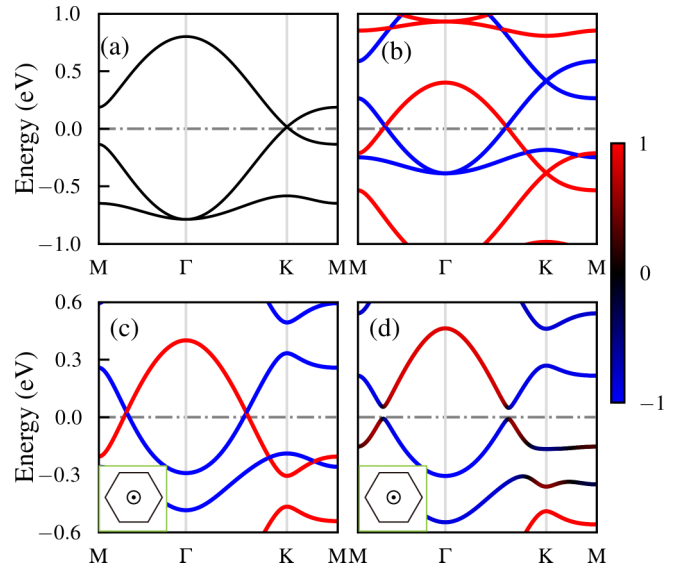


FIG. 5. Evolution of TB band structures of the CeCl single layer. The red (blue) color of color bar represent the weights of spin-up (spin-down) channel. (a) When exchange field \mathbf{m} and SOC are both excluded, the spin up and down of the CeCl single layer are degenerate. (b) When only \mathbf{m} is included, the spin degeneracy of band structure is broken, and a Weyl nodal loop is formed near the Fermi energy. (c) When \mathbf{m} along the z direction and SOC term H_{SO} are included, the Weyl nodal loop formed by different spins is still retained, while other points contributed by the same spin are gapped. (d) When both \mathbf{m} along the z direction and SOC term H_{SO} are included, the Weyl nodal loop is completely gapped. $t_m = -0.4$ eV and $\lambda_{SO} = 0.1$ eV in (b), (c), and (d).

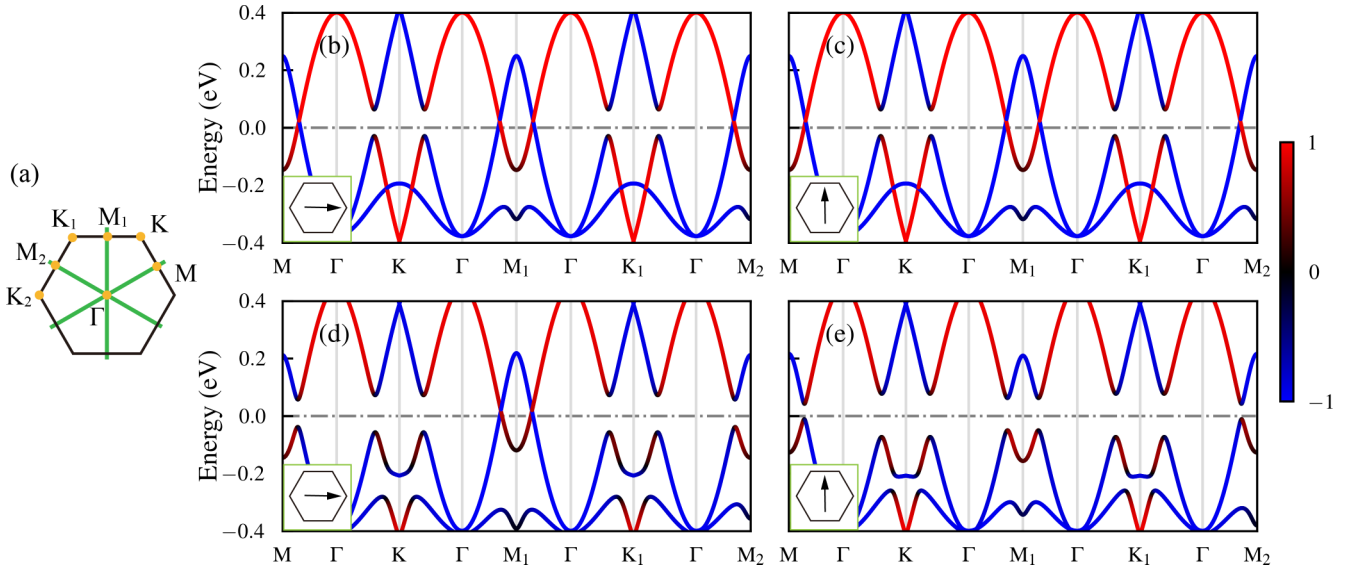


FIG. 6. Evolution of TB band structures when exchange field \mathbf{m} along the x or y direction and SOC are considered. The red (blue) color of color bar represent the weights of spin up (down). (a) The corresponding Brillouin zone without SOC. The yellow dots represent high-symmetry points, and green lines represent mirror planes perpendicular to the x - y plane. (b), (c) The TB band structures when SOC term $H_{SO'}$ and \mathbf{m} are considered. (d), (e) The TB band structures when SOC term H_{SO} and \mathbf{m} are considered. The \mathbf{m} is along the x direction for (b) and (d), and along the y direction for (c) and (e). $t_m = -0.4$ eV and $\lambda_{SO} = 0.1$ eV in (b)–(e).

shows that a Dirac cone appears at the K point. When only \mathbf{m} is applied, the spin degeneracy is broken, the spin-up (down) bands shift downward (upward), and a Weyl nodal loop is formed near the Fermi energy, as shown in Fig. 5(b). Furthermore, we consider the influence of \mathbf{m} along the z direction (i.e., $\mathbf{m} \cdot \boldsymbol{\sigma} = \sigma_z$) and SOC. When SOC is included further, we first assume that the lack of coupling between d_2 and d_0 , as well as between d_2 and d_1 , and this assumed SOC term will be expressed as

$$H_{SO'} = \lambda_{SO} \begin{pmatrix} 0 & 0 & 0 & 0 & 0 \\ 0 & -2i\sigma_z & 0 & 0 & 0 \\ & 0 & 0 & 0 & 0 \\ & & & 0 & i\sigma_z \\ \text{H.c.} & & & & 0 \end{pmatrix}.$$

Obviously these matrix elements are only contributed by σ_z that can not flip spin. As shown in Fig. 5(c), the Weyl nodal loop is retained, while other degenerate points contributed by same spin open the gap. If the SOC term is H_{SO} which has more coupling than $H_{SO'}$, its matrix elements have additional σ_x and σ_y that flip spin and induce the hybridization between spin-up and spin-down components. The Weyl nodal loop with different spin contributions is completely gapped, as shown in Fig. 5(d).

When the exchange field \mathbf{m} is along the x direction, $\mathbf{m} \cdot \boldsymbol{\sigma} = \sigma_x$ can also induce the hybridization between spin components, which only contributes in the same orbitals because of the on-site exchange field. We first consider the evolution of the band structure when exchange field \mathbf{m} along x and $H_{SO'}$ are considered. As shown in Fig. 6(b), the band structure is gapped in the path Γ -K and Γ -K₁, but is gapless in the path Γ -M, Γ -M₁, and Γ -M₂. Furthermore, by replacing $H_{SO'}$ with H_{SO} , the coupling of d_0 (d_1) and d_2 is introduced, and the gapless band structure is completely gapped except the path

Γ -M₁ where the mirror symmetry is preserved, as shown in Fig. 6(d).

When the exchange field \mathbf{m} is along the y direction, $\mathbf{m} \cdot \boldsymbol{\sigma} = \sigma_y$ has the same effect as σ_x . When considering $H_{SO'}$, the evolution of the band structure is the same for both the case when the exchange field \mathbf{m} is along y and the case when it is along x , as shown Fig. 6(c). Furthermore, by replacing $H_{SO'}$ with H_{SO} to introduce the coupling of d_0 (d_1) and d_2 , the gapless band structure is completely gapped [see Fig. 6(e)].

If only $H_{SO'}$ is considered, the coupling between d_0 (d_1) and d_2 is lacking. Whether the exchange field \mathbf{m} is along z , x , or y direction, the Weyl nodal loop cannot be completely gapped. When the actual term H_{SO} is considered to introduce the coupling between d_0 (d_1) and d_2 , it is consistent with DFT calculations. As discussed in DFT calculations, when \mathbf{m} is along the z or y direction, all mirror symmetries are broken, and a global gap exists in the Weyl nodal loop. When \mathbf{m} is along the x direction, only the mirror symmetry perpendicular to \mathbf{m} is retained, and a gapless band structure is in the path Γ -M₁. Although the Weyl nodal loop is mainly contributed by the d_0 and d_1 orbitals, the coupling between d_2 and these orbitals plays a key role in the gap of the Weyl nodal loop. As the in-plane magnetization direction rotates, the Berry curvature and Chern number also change periodically (see Fig. S7 [52]).

This TB model based on the Slater-Koster framework may be generalized to explain the Weyl nodal loop in other lanthanide monohalides LnX ($Ln = \text{La}$ [34,58,65,66], Pr, Nd, Sm, Gd [58,67], Tb [68], Dy, Ho, Er, Tm, Lu; $X = \text{Cl, Br, I}$) single layers, which is contributed by d orbitals of Ln.

VI. CONCLUSION

Based on first-principles calculations and the TB model, we theoretically predict 2D ferromagnetic single-layers CeX

with isotropic in-plane magnetocrystalline anisotropy energy and abundant topological states. These materials with dynamical stability have isotropic magnetocrystalline anisotropy energy in the x - y plane. CeCl and CeBr single layers have in-plane magnetization in the ground state while the magnetization prefers the out-of-plane for CeI single layers. When SOC is ignored, these single layers are 2D Weyl nodal loop semimetals with the nodal loop contributed by different spins. When SOC is considered, if the magnetization maintains a mirror symmetry, the Weyl nodal loop degenerates into twofold degenerate Weyl points and CeX single layers transform into 2D Weyl semimetals. Conversely, if the magnetization breaks all mirror symmetries, the Weyl points are gapped. Simultaneously, the breaking of both $\mathcal{T} \otimes \mathcal{M}_z$ and $\mathcal{T} \otimes \mathcal{M}_z \otimes \mathcal{I}$ symmetries and the band gap in the Weyl nodal loop leads to the QAH state in the system. Rotating the in-plane magnetization direction within the isotropic x - y plane results in corresponding change in the broken degree

of mirror symmetry, which alters the band gap of the Weyl nodal loop in high-symmetry paths, Berry curvature, and the sign of Chern number periodically. Finally, a TB model is further constructed to explain the origin of these nontrivial band structures. These findings illustrate that CeX single layers with tunable QAH states are promising candidates for future low-power spintronic devices.

ACKNOWLEDGMENTS

This work was supported by the National Natural Science Foundation of China (Grant No. 11874092), the Fok Ying-Tong Education Foundation, China (Grant No. 161005), the Science Fund for Distinguished Young Scholars of Hunan Province (Grant No. 2021JJ10039), and the Postgraduate Scientific Research Innovation Project of Hunan Province (Grant No. CX20230930).

-
- [1] N. B. Kopnin, T. T. Heikkilä, and G. E. Volovik, *Phys. Rev. B* **83**, 220503(R) (2011).
- [2] C.-Z. Chang, J. Zhang, X. Feng, J. Shen, Z. Zhang, M. Guo, K. Li, Y. Ou, P. Wei, L.-L. Wang, Z.-Q. Ji, Y. Feng, S. Ji, X. Chen, J. Jia, X. Dai, Z. Fang, S.-C. Zhang, K. He, Y. Wang *et al.*, *Science* **340**, 167 (2013).
- [3] H. Jiang, Z. Qiao, H. Liu, and Q. Niu, *Phys. Rev. B* **85**, 045445 (2012).
- [4] X. Liu, H.-C. Hsu, and C.-X. Liu, *Phys. Rev. Lett.* **111**, 086802 (2013).
- [5] S.-C. Wu, G. Shan, and B. Yan, *Phys. Rev. Lett.* **113**, 256401 (2014).
- [6] J. Zhang, B. Zhao, T. Zhou, Y. Xue, C. Ma, and Z. Yang, *Phys. Rev. B* **97**, 085401 (2018).
- [7] Y. Hou, J. Kim, and R. Wu, *Sci. Adv.* **5**, eaaw1874 (2019).
- [8] J. He, X. Li, P. Lyu, and P. Nachtigall, *Nanoscale* **9**, 2246 (2017).
- [9] X.-L. Sheng and B. K. Nikolić, *Phys. Rev. B* **95**, 201402(R) (2017).
- [10] X. Kong, L. Li, O. Leenaerts, W. Wang, X.-J. Liu, and F. M. Peeters, *Nanoscale* **10**, 8153 (2018).
- [11] Y. Deng, Y. Yu, M. Z. Shi, Z. Guo, Z. Xu, J. Wang, X. H. Chen, and Y. Zhang, *Science* **367**, 895 (2020).
- [12] H. Fu, C.-X. Liu, and B. Yan, *Sci. Adv.* **6**, eaaz0948 (2020).
- [13] W. Zhu, C. Song, L. Liao, Z. Zhou, H. Bai, Y. Zhou, and F. Pan, *Phys. Rev. B* **102**, 085111 (2020).
- [14] Y. Ren, J. Zeng, X. Deng, F. Yang, H. Pan, and Z. Qiao, *Phys. Rev. B* **94**, 085411 (2016).
- [15] P. Zhong, Y. Ren, Y. Han, L. Zhang, and Z. Qiao, *Phys. Rev. B* **96**, 241103(R) (2017).
- [16] X. Zhou, R.-W. Zhang, Z. Zhang, D.-S. Ma, W. Feng, Y. Mokrousov, and Y. Yao, *J. Phys. Chem. Lett.* **10**, 3101 (2019).
- [17] L. Jin, L. Wang, X. Zhang, Y. Liu, X. Dai, H. Gao, and G. Liu, *Nanoscale* **13**, 5901 (2021).
- [18] S. Li, X. Li, W. Ji, P. Li, S. Yan, and C. Zhang, *Phys. Chem. Chem. Phys.* **25**, 18275 (2023).
- [19] Z. Li, Y. Han, and Z. Qiao, *Phys. Rev. Lett.* **129**, 036801 (2022).
- [20] X. Wu, R. Li, X. Zou, B. Huang, Y. Dai, and C. Niu, *Phys. Rev. B* **108**, 115438 (2023).
- [21] X. Xu, T. Guo, D. Guan, J. Li, A. He, J. Lu, X. Yao, Y. Liu, and X. Zhang, *Phys. Rev. B* **108**, 214427 (2023).
- [22] X. Xu, T. Guo, Y. Liu, A. Chen, X. Zhu, S. Wang, A. He, J. Lu, Y. Liu, and X. Zhang, *Appl. Phys. Lett.* **123**, 163103 (2023).
- [23] J.-Y. You, C. Chen, Z. Zhang, X.-L. Sheng, S. A. Yang, and G. Su, *Phys. Rev. B* **100**, 064408 (2019).
- [24] X. Zhang, Y. Li, T. He, M. Zhao, L. Jin, C. Liu, X. Dai, Y. Liu, H. Yuan, and G. Liu, *Phys. Rev. B* **108**, 054404 (2023).
- [25] Y. Yu, X. Chen, X. Liu, J. Li, B. Sanyal, X. Kong, F. M. Peeters, and L. Li, *Phys. Rev. B* **105**, 024407 (2022).
- [26] X. L. Wang, *Phys. Rev. Lett.* **100**, 156404 (2008).
- [27] Z. Liu, J. Liu, and J. Zhao, *Nano Res.* **10**, 1972 (2017).
- [28] X. Wang, T. Li, Z. Cheng, X.-L. Wang, and H. Chen, *Appl. Phys. Rev.* **5**, 041103 (2018).
- [29] Y. Kim, B. J. Wieder, C. L. Kane, and A. M. Rappe, *Phys. Rev. Lett.* **115**, 036806 (2015).
- [30] J.-M. Carter, V. V. Shankar, M. A. Zeb, and H.-Y. Kee, *Phys. Rev. B* **85**, 115105 (2012).
- [31] Y. Jiao, F. Ma, C. Zhang, J. Bell, S. Sanvito, and A. Du, *Phys. Rev. Lett.* **119**, 016403 (2017).
- [32] R. Wang, J. Z. Zhao, Y. J. Jin, Y. P. Du, Y. X. Zhao, H. Xu, and S. Y. Tong, *Phys. Rev. B* **97**, 241111(R) (2018).
- [33] C. Chen, Z.-M. Yu, S. Li, Z. Chen, X.-L. Sheng, and S. A. Yang, *Phys. Rev. B* **99**, 075131 (2019).
- [34] Z. Liu, G. Zhao, B. Liu, Z. F. Wang, J. Yang, and F. Liu, *Phys. Rev. Lett.* **121**, 246401 (2018).
- [35] S. Zhang, X. Zhang, Z. He, L. Jin, C. Liu, Y. Liu, and G. Liu, *Nanoscale* **15**, 14018 (2023).
- [36] G. Kresse and J. Furthmüller, *Comput. Mater. Sci.* **6**, 15 (1996).
- [37] G. Kresse and J. Furthmüller, *Phys. Rev. B* **54**, 11169 (1996).
- [38] P. E. Blöchl, *Phys. Rev. B* **50**, 17953 (1994).
- [39] G. Kresse and D. Joubert, *Phys. Rev. B* **59**, 1758 (1999).
- [40] J. P. Perdew, K. Burke, and M. Ernzerhof, *Phys. Rev. Lett.* **77**, 3865 (1996).
- [41] H. J. Monkhorst and J. D. Pack, *Phys. Rev. B* **13**, 5188 (1976).

- [42] S. L. Dudarev, G. A. Botton, S. Y. Savrasov, C. J. Humphreys, and A. P. Sutton, *Phys. Rev. B* **57**, 1505 (1998).
- [43] S. Lutfalla, V. Shapovalov, and A. T. Bell, *J. Chem. Theory Comput.* **7**, 2218 (2011).
- [44] A. Togo and I. Tanaka, *Scr. Mater.* **108**, 1 (2015).
- [45] G. Pizzi, V. Vitale, R. Arita, S. Blügel, F. Freimuth, G. Géranton, M. Gibertini, D. Gresch, C. Johnson, T. Koretsune, J. Ibañez-Azpiroz, H. Lee, J.-M. Lihm, D. Marchand, A. Marrazzo, Y. Mokrousov, J. I. Mustafa, Y. Nohara, Y. Nomura, L. Paulatto *et al.*, *J. Phys.: Condens. Matter* **32**, 165902 (2020).
- [46] Q. Wu, S. Zhang, H.-F. Song, M. Troyer, and A. A. Soluyanov, *Comput. Phys. Commun.* **224**, 405 (2018).
- [47] H.-J. Kim, VASPBERRY, <https://github.com/Infant83/VASPBERRY> (2018).
- [48] S.-W. Kim, H.-J. Kim, S. Cheon, and T.-H. Kim, *Phys. Rev. Lett.* **128**, 046401 (2022).
- [49] H. T. Stokes, D. M. Hatch, and B. J. Campbell, FINDSYM, ISOTROPY Software Suite, <https://iso.byu.edu/iso> (2022).
- [50] K. Momma and F. Izumi, *J. Appl. Crystallogr.* **44**, 1272 (2011).
- [51] H. J. Mattausch, A. Simon, N. Holzer, and R. Eger, *Z. Anorg. Allg. Chem.* **466**, 7 (1980).
- [52] See Supplemental Material at <http://link.aps.org/supplemental/10.1103/PhysRevB.109.115418> for the phonon spectrums, molecular dynamics calculations, magnetic properties, orbital-projected band structures, and topological properties of CeX single layers, which includes Refs. [69–71].
- [53] W.-B. Zhang, Q. Qu, P. Zhu, and C.-H. Lam, *J. Mater. Chem. C* **3**, 12457 (2015).
- [54] X. Jiang, Q. Liu, J. Xing, N. Liu, Y. Guo, Z. Liu, and J. Zhao, *Appl. Phys. Rev.* **8**, 031305 (2021).
- [55] M. Getzloff, *Fundamentals of Magnetism* (Springer, Berlin, Heidelberg, 2008).
- [56] M. Bonilla, S. Kolekar, Y. Ma, H. C. Diaz, V. Kalappattil, R. Das, T. Eggers, H. R. Gutierrez, M.-H. Phan, and M. Batzill, *Nat. Nanotechnol.* **13**, 289 (2018).
- [57] X. Feng, J. Zhu, W. Wu, and S. A. Yang, *Chin. Phys. B* **30**, 107304 (2021).
- [58] S. Nie, H. Weng, and F. B. Prinz, *Phys. Rev. B* **99**, 035125 (2019).
- [59] W. A. Harrison, *Elementary Electronic Structure* (World Scientific, Singapore, 1999).
- [60] S. Konschuh, M. Gmitra, and J. Fabian, *Phys. Rev. B* **82**, 245412 (2010).
- [61] C.-C. Liu, H. Jiang, and Y. Yao, *Phys. Rev. B* **84**, 195430 (2011).
- [62] Y. Liu and R. E. Allen, *Phys. Rev. B* **52**, 1566 (1995).
- [63] J. C. Slater and G. F. Koster, *Phys. Rev.* **94**, 1498 (1954).
- [64] H.-J. Kim, TBFIT, <https://github.com/Infant83/TBFIT> (2018).
- [65] L. Jin, X. Zhang, T. He, W. Meng, X. Dai, and G. Liu, *Appl. Surf. Sci.* **520**, 146376 (2020).
- [66] M. Wu, *2D Mater.* **4**, 021014 (2017).
- [67] C. Chen, L. Fang, G. Zhao, X. Liu, J. Wang, L. A. Burton, Y. Zhang, and W. Ren, *J. Mater. Chem. C* **9**, 9539 (2021).
- [68] H. Xu, Y. Jiang, H. Wang, and J. Wang, *Phys. Rev. B* **109**, 035122 (2024).
- [69] X. Wang, J. R. Yates, I. Souza, and D. Vanderbilt, *Phys. Rev. B* **74**, 195118 (2006).
- [70] D. Xiao, M.-C. Chang, and Q. Niu, *Rev. Mod. Phys.* **82**, 1959 (2010).
- [71] M. Gradhand, D. V. Fedorov, F. Pientka, P. Zahn, I. Mertig, and B. L. Györfy, *J. Phys.: Condens. Matter* **24**, 213202 (2012).